J. Applied Membrane Science & Technology, Vol. 30, August 2026, 180-197

Hydrothermally Synthesized $CoMn_2O_4$/Graphite Composite as a High-Capacity Anode for Lithium-Ion Batteries

Jia Xiao Li[1], Muhammad Norhaffis Mustafa[2], Farhana Syakirah Ismail[2], Nur Hawa Nabilah Azman[2], Muhammad Amirul Aizat Mohd Abdah[1*]

[1]Department of Chemistry, Faculty of Science, University Teknologi Malaysia, 81310 UTM Johor Bahru, Johor, Malaysia
[2]Sunway Centre for Electrochemical Energy and Sustainable Technology, Faculty of Engineering and Technology, Sunway University, No. 5, Jalan University, Bandar Sunway, 47500 Subang Jaya, Selangor, Malaysia

ubmitted: 29/06/2026. Revised edition: 27/07/2026. Accepted: 27/07/2026. Available online: 21/08/2026

ABSTRACT

The increasing demand for high-energy-density lithium-ion batteries (LIBs) drives the development of anode materials with capacities exceeding that of graphite (372 mAh g^{-1}). $CoMn_2O_4$, with a high theoretical capacity (921 mAh g^{-1}), is a promising candidate but suffers from low conductivity and severe volume expansion. In this work, a $CoMn_2O_4$/graphite (CMO/g) composite is developed to address these limitations through a synergistic effect. $CoMn_2O_4$ is synthesized via a hydrothermal method followed by calcination, and the sample treated at 700 °C exhibits the best crystallinity and morphology. Structural characterizations (XRD, FTIR, FESEM-EDX) confirm the successful formation of the composite and uniform distribution of $CoMn_2O_4$ on graphite. Electrochemical evaluations reveal that CMO/g-3 delivers a high initial discharge capacity of 2503 mAh g^{-1} and maintains ~1000 mAh g^{-1} after 100 cycles with nearly 100% coulombic efficiency and low charge-transfer resistance. A full cell assembled with CMO/g-3 and $LiFePO_4$ provides an initial discharge capacity of 146.5 mAh g^{-1} at 0.2 A g^{-1}, although capacity fading occurs upon prolonged cycling due to volume expansion effects. Overall, the $CoMn_2O_4$/graphite composite demonstrates enhanced electrochemical performance and promising potential as a high-capacity anode material for next-generation LIBs.

Keywords: $CoMn_2O_4$; Hydrothermal method; Anode materials; Graphite; Lithium-ion batteries

1.0 INTRODUCTION

In recent years, global economic development has led to a constant rise in energy demand. However, fossil fuels cannot sustainably meet this increasing energy demand, resulting in a widening gap between supply and demand. Moreover, excessive use of fossil fuels, including coal, oil, and natural gas, has caused serious environmental problems and a global energy crisis[1]. In order to overcome this challenge, it has become urgent to restructure a cleaner and more renewable energy system. Renewable energy sources (RES) have been increasing their presence in the power field and have become great substitutes

* Corresponding to: M. A. A. Mohd Abdah (email: muhammadamirulaizat@utm.my)
DOI: https://doi.org/10.11113/jamst.v30n2.352

for fossil fuels, with advances in technology[2]. However, RES, such as solar and wind, face the problems of intermittency and instability, which make it difficult to maintain a reliable and continuous power supply[3, 4]. Energy storage technology (EST) is one of the key technologies to overcome the limitations of RES[5].

Among all kinds of EST, Lithium-ion batteries (LIBs) have become the dominant energy storage device due to their exceptional attributes such as high energy density, elevated operating voltage, good capability of security, and environmental friendliness[6, 7]. By storing excess energy during periods of surplus generation and releasing it during peak periods, LIBs effectively mitigate the fluctuations of solar and wind energy. The principle of LIB is that Li^+ continuously intercalates and extracts between the anode and cathode, undergoing oxidation-reduction reactions to store and release electric energy. LIBs have an interesting nickname, "rocking chair batteries", because Li^+ could shuttle back and forth between the electrodes, just like a rocking chair swaying rhythmically. At the same time, the rapid increase of electrical vehicle (EV) is accelerating the transition of energy sources in the field of transportation and reducing greenhouse gas emissions[4]. However, with the development of the EV industry and the growing demand for energy storage systems, higher performance requirements have been placed on LIBs [8].

The conventional graphite anode is insufficient to meet the demand of high-performance batteries due to its limited theoretical capacity of 372 mAh g^{-1}, which remains a critical factor constraining the development of lithium-ion batteries [9, 10]. Currently, promising anode materials under development include bimetallic transition metal oxides (BTMOs), and carbon-based composite materials. BTMOs are being explored as next-generation substitutes for graphite, and they exhibit better electrochemical performance than TMOs. BTMOs exhibit higher charge storage capability than TMOs due to their multiple oxidation states, which enable them to store more charges. However, BTMOs electrode is still insufficient to meet the market standards of LIBs due to volume change during the cycling processes.

Previous studies also demonstrated the limitations of BTMO-based LIBs in terms of cycling performance. For instance, prior research has shown a rapid capacity decay of $CoMn_2O_4$ electrodes, with the discharge capacity dropping to just 142 mAh g^{-1} after 100 cycles at 0.1 A g^{-1}[11]. These findings suggest that severe volume change in BTMOs materials makes it less suitable for long-term application in commercial LIBs. To synthesize carbon-based BTMOs composites could effectively address the electrochemical limitations of BTMOs by enhancing electrical conductivity and structural stability. At present, this approach has been a promising strategy for applications such as LIB, supercapacitors, and catalysis.

Among all BTMOs, $CoMn_2O_4$ is considered a highly promising anode material with superior electrochemical performance. $CoMn_2O_4$ has been considered as one of the most desirable electrode materials in LIBs and supercapacitors. According to previous studies, $CoMn_2O_4$ exhibits a high theoretical capacity of 921 mAh $g^{-1,}$ much higher than that of the commercialized graphite (372 mAh g^{-1}). In a previous study, the $CoMn_2O_4$ electrode has been prepared successfully. This electrode showed good discharge specific capacity of 733 mAh g^{-1} at a current density of 0.2 A g^{-1} after 100 cycles based on the effect of the synthetic strategies between Co and Mn[12]. In another research, $CoMn_2O_4$ and $MnCo_2O_4$ nanopowder were synthesized by the co-precipitation method; the $CoMn_2O_4$ electrode exhibited an initial discharge capacity(~1710 mAh g^{-1}) higher than that of (~1443 mAh g^{-1}) for the $MnCo_2O_4$ electrode at a current density of 0.1 A g^{-1}[8].

* Corresponding to: M. A. A. Mohd Abdah (email: muhammadamirulaizat@utm.my)
DOI: https://doi.org/10.11113/jamst.v30n2.352

However, like other transition metal oxides, the $CoMn_2O_4$ electrode cannot satisfy the requirements of the market due to its severe volume change and poor electrical conductivity. A combination of carbon materials and $CoMn_2O_4$ is a promising method to overcome the above shortcomings. Recently, carbon-based BTMOs composites as the electrode materials for LIBs have received more and more attention from lots of researchers. BTMOs have shown excellent electrochemical performance among various electrode materials, while their exhibits severe volume change and poor electrical conductivity, leading to a significant capacity fade during cycling processes and poor cycling stability, which makes it difficult to meet the requirements of practical applications. Carbon materials exhibit excellent conductivity and superior stability, which can effectively compensate for the shortcomings of BTMOs. Recently, researchers have proposed the combination of carbon materials with BTMOs to synthesize composite electrode materials. It has been demonstrated that this type of composite electrode material exhibits superior electrochemical performance with high specific capacity and better stability than pure BTMOs.

Herein, we report the preparation of BTMOs with carbon-based materials as an anode for LIBs. This work offers a promising approach for developing high-performance LIB anodes, and this strategy not only preserves the high theoretical specific capacity of BTMOs but also takes advantage of the high conductivity and flexibility of carbon-based materials to address the poor electrical conductivity of BTMOs. In addition, the composite of BTMOs and carbon exhibits a higher capacity than pure BTMOs due to the creation of more electroactive sites, resulting from the increased surface area of the carbon-based materials. This highlights a positive synergistic effect between the carbon materials and BTMOs, which improves the overall electrochemical performance of electrode materials. Therefore, carbon-based BTMOs composites show great application potential as an anode for LIBs.

2.0 EXPERIMENTAL

2.1 Materials

Cobalt acetate tetrahydrate ($Co(CH_3COO)_2 \cdot 4H_2O$) and manganese (II) sulphate monohydrate ($MnSO_4 \cdot 4H_2O$) were purchased from QreC. Urea and lithium hexafluorophosphate ($LiPF_6$) in ethylene carbonate (EC) and dimethyl carbonate (DMC) were obtained from Sigma-Aldrich. Graphite powder and N-methyl-2-pyrrolidone (NMP) were attained from R&M Chemicals. Lithium iron phosphate ($LiFePO_4$) was purchased from International Battery Center Sdn. Bhd, Malaysia. Solef® and Super P® were procured fromSolvay Specialty Chemicals Asia Pacific Ltd, Singapore, and KGC Resources Sdn Bhd, Malaysia, respectively. Deionized water (DI) with a resistivity of 10 MΩ·cm was used throughout the experiment as the solvent.

2.2 Preparation of $CoMn_2O_4$/graphite

$CoMn_2O_4$ was prepared by dissolving 9.96 g of $Co(CH_3COO)_2 \cdot 4H_2O$, 17.84 g of $MnSO_4 \cdot 4H_2O$, and 2.40 g of urea in 400 mL of DI water. The molar ratio of $Co(CH_3COO)_2 \cdot 4H_2O$, $MnSO_4 \cdot 4H_2O$, and urea was maintained at 1:2:1. The mixture was

* Corresponding to: M. A. A. Mohd Abdah (email: muhammadamirulaizat@utm.my)
DOI: https://doi.org/10.11113/jamst.v30n2.352

stirred at room temperature until a homogeneous solution was obtained. After that, the mixture was moved to a 400 ml Teflon-lined stainless steel autoclave and heated at 180°C for 12 hours. After that, the precipitates were centrifuged, washed, and dried in an oven at 60°C for 12 hours. The powder was calcined to obtain $CoMn_2O$ at different temperatures of 400, 500, 600, and 700°C at a heating rate of 2°C min^{-1} for 2 hours and were denoted as CMO-400, CMO-500, CMO-600, CMO-700, respectively. The $CoMn_2O_4$/graphite was prepared by blending $CoMn_2O_4$ and graphite at various molar ratios, followed by grinding in a mortar. The molar ratios of $CoMn_2O_4$:graphite include 0:10, 1:9, 2:8 and 3:7, and labeled as CMO/g-0, CMO/g-1, CMO/g-2, and CMO/g-3, respectively. The overall experimental procedure is depicted in Figure 1, which outlines the hydrothermal synthesis of $CoMn_2O_4$ as well as the fabrication of $CoMn_2O_4$/graphite composite electrodes.

2.3 Fabrication of $CoMn_2O_4$/graphite Electrodes

The slurry of $CoMn_2O_4$/graphite was prepared by mixing 85 *wt*% $CoMn_2O_4$/graphite, 5 *wt*% Super P® carbon, and 10 *wt*% PVDF in NMP, serving as the active material, conductive agent, and binder, respectively[13]. The slurry was then coated onto the surface of Cu foil using an automatic film coater with a fixed coating speed and a 150 µm doctor blade gap to achieve a uniform coating thickness. Then the slurry was dried in an oven at 60°C for 12 hours. Four different ratios of $CoMn_2O_4$/graphite were investigated to determine the optimal mixing ratio for further applications. After drying, electrodes were punched from the central region of the coated films to minimize edge effects. The prepared electrodes had a diameter of 16 mm (geometric area = 2.01 cm^2), with material masses of 25 mg (CMO/g-0), 23 mg (CMO/g-1), 23 mg (CMO/g-2), and 23 mg (CMO/g-3), corresponding to electrode loadings of 12.44, 11.45, 11.45, and 11.45 mg cm^{-2}, respectively. The $CoMn_2O_4$/graphite electrode was assembled in a coin cell with $CoMn_2O_4$/graphite as the working electrode, lithium metal as the counter electrode, Celgard® 2400 membrane as the separator, a spacer, and a spring. Figure 2 illustrates the assembly procedure of CR2032 type coin cells, which was conducted inside an argon-atmosphere glove box.

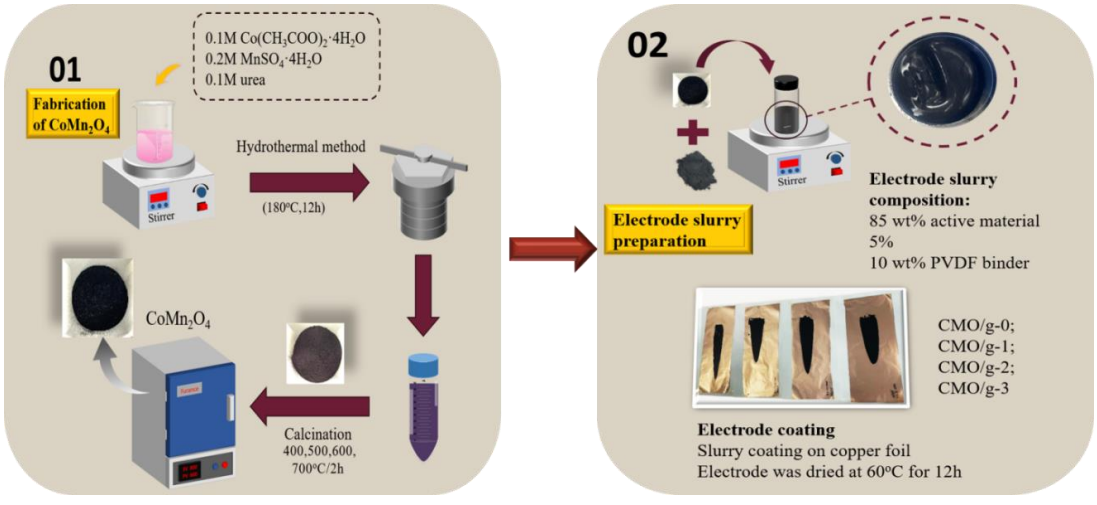

Figure 1 Schematic illustration of the hydrothermal synthesis of $CoMn_2O_4$ and the subsequent preparation of $CoMn_2O_4$/graphite electrodes

* Corresponding to: M. A. A. Mohd Abdah (email: muhammadamirulaizat@utm.my)
DOI: https://doi.org/10.11113/jamst.v30n2.352

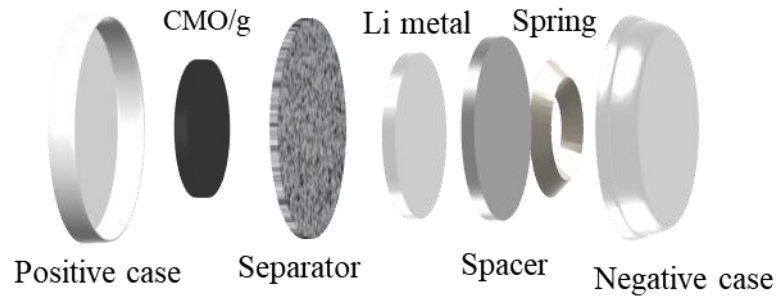

Figure 2. The schematic illustration of CR2032 type coin cell

2.4 Physicochemical Characterizations

The functional groups and the existence of particular chemical bonds in the as-synthesized anode materials were determined using a Fourier Transform Infrared Spectrometer (FTIR). Field Emission Scanning Electron Microscopy (FESEM) equipped with Energy-Dispersive X-ray Spectroscopy (EDX) was used to study surface morphology and the elemental distribution on the as-synthesized anode materials, respectively. The specific surface area of anode materials which is a key parameter affecting electrochemical performance, were identified via the Brunauer–Emmett–Teller (BET) method using a Micromeritics TriStar II analyzer. The crystallinity of the as-synthesized anode materials was examined using an X-ray diffractometer (XRD). In addition, the Debye-Scherer formula was applied to evaluate the crystallite size of the synthesized electrode materials based on equation (1):

$$d = \frac{0.9\lambda}{\beta cos\theta} \quad (1)$$

Where λ is the X-ray wavelength, β is the full width at half maximum of the diffraction peak, θ refers to the Bragg angle, and d corresponds to the crystallite size [8].

2.5 Electrochemical Characterizations

The electrochemical performances of the assembled coin cells were measured using galvanostatic charge-discharge (GCD) at various current densities of 0.1 A g^{-1} in the voltage range of 0.01–3.0 V (*vs*. Li/Li^+). Cyclic voltammetry (CV) measurements were performed in the voltage range of 0.0–3.0 V *vs.* Li/Li^+ at a scanning rate of 0.1 mV s^{-1}, and electrochemical impedance spectroscopy (EIS) with frequency ranging from 100 kHz to 1 Hz at 10 mV amplitude. As for the full-cell testing, CMO/g-3 and lithium iron phosphate ($LiFePO_4$) were employed as the anode and cathode, respectively. Prior to cell assembly, both electrodes underwent electrochemical pre-discharge and pre-charge treatments to suppress SEI-related effects and achieve a stabilized electrochemical state. GCD cycling for the full cell was carried out using the same battery testing system with a cutoff voltage from 1.2 to 4.2 V (*vs.* Li^+/Li) at a current density of 0.2 A g^{-1}.

* Corresponding to: M. A. A. Mohd Abdah (email: muhammadamirulaizat@utm.my)
DOI: https://doi.org/10.11113/jamst.v30n2.352

3.0 RESULTS AND DISCUSSION

3.1 Structural Properties

Figure 3 displays the XRD patterns of the as-synthesized anode, and the XRD pattern (Figure 3a) of CMO-400 does not match well with the standard pattern of $CoMn_2O_4$ (JCPDF No. 77-0471), indicating that the calcination temperature of 400°C is insufficient to synthesize pure-phase $CoMn_2O_4$. The CMO calcined at 500, 600, and 700°C exhibit similar diffraction peaks with main diffraction peaks located at 2θ = 18.2, 33.0, 36.3, and 60.7°, respectively, corresponded to the reflection planes (101), (103), (221), and (224), respectively (JCPDF No. 77-0471). The crystallite size was estimated using the Debye–Scherrer equation based on the most intense diffraction peak at 2θ = 36.3°[8].

With increasing calcination temperature from 500 to 700ºC, the peaks became sharper and narrower, indicating the crystallinity of $CoMn_2O_4$ improves with increasing temperature. Meanwhile, all the diffraction peaks of the $CoMn_2O_4$ treated at 700°C were well indexed with the tetragonal spinel structure of $CoMn_2O_4$, indicating the total transformation from CMO precursor to $CoMn_2O_4$. As expected, CMO-700 exhibited a smaller crystalline size of 10 nm, while CMO-600 showed a significantly larger size of 49 nm. The smaller crystalline size could provide a higher surface area, whereas crystalline size may lead to increased side reactions and structural instability. Considering that graphite was later introduced to improve the stability, CMO-700 was selected as the optimal sample for subsequent studies on composite ratio optimization[8].

The crystal structure of CMO/g-3 was further investigated by XRD analysis within the diffraction angle 10º-90º. As shown in Figure 3b, the diffraction peaks fit well with graphite (JCPDF No. 41-1487) and spinal $CoMn_2O_4$ (JCPDF No. 89-7412), indicating successful mixing of graphite and $CoMn_2O_4$ [14]. All of diffraction peaks of $CoMn_2O_4$ are clearly observed in CMO/g-3 electrode, suggesting that the crystal structure of $CoMn_2O_4$ is well preserved after mixing, which is consistent with the FTIR result of CMO/g-3 electrode.

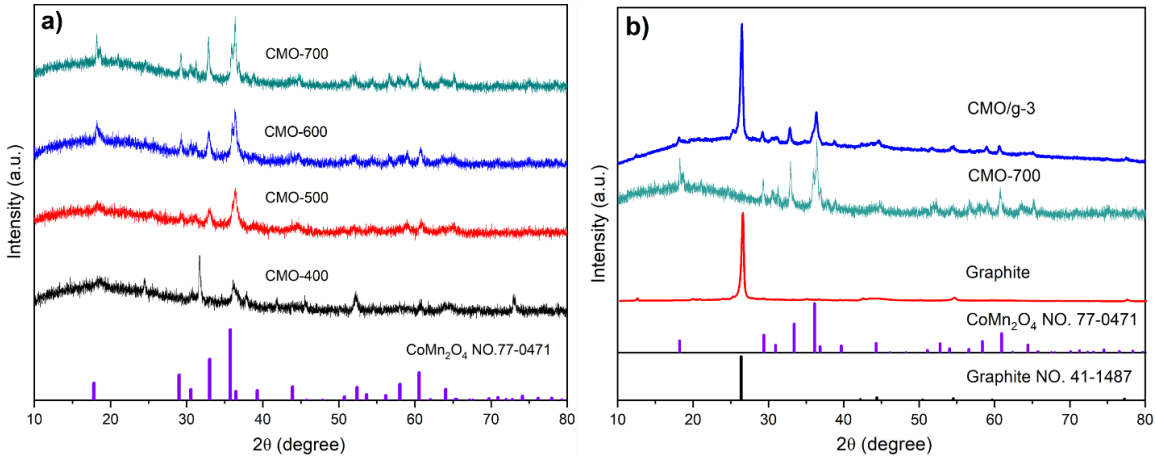

Figure 3. (a) XRD spectra of CMO-400, CMO-500, CMO-600, and CMO-700. (b) XRD spectra of graphite, CMO, and CMO/g-3

* Corresponding to: M. A. A. Mohd Abdah (email: muhammadamirulaizat@utm.my)
DOI: https://doi.org/10.11113/jamst.v30n2.352

Figure 4 displays the FTIR spectra of $CoMn_2O_4$ obtained at various calcined temperatures and CMO/g-3. The peaks at 3411.5 and 1630.3 cm^{-1} were attributed to -OH stretching and bending, respectively, due to absorbed water molecules on the surface[15]. Several peaks appeared in the region of 1000-1200 $cm^{-1,}$ which were attributed to the C-O and C-N stretching vibrations, which were associated with residual organic species from incompletely decomposed organic precursors. These peaks were clearly visible in CMO-400 and CMO-500 samples. However, the intensity of peaks significantly increased when the calcination temperature rose to 600°C and above. This trend indicates a more thorough decomposition of the precursor at high calcined temperature.

In addition, a peak located at 856.4 cm^{-1} was related to the bending vibration of C-H bonds in residual acetate groups. The disappearance of this peak in the samples calcined at higher temperatures further supported the effective removal of organic residues under high-temperature conditions. More importantly, two characteristic adsorption peaks of the spinal $CoMn_2O_4$ were observed at 602.5 cm^{-1} and 508.2 cm^{-1}, corresponding to Co-O and Mn-O bending vibrations, respectively. These peaks were weak in CMO-400 sample, suggesting pure-phase $CoMn_2O_4$ cannot be formed at low temperature. While sharp and wide peaks clearly appeared in CMO-600 and CMO-700 samples.

Compared with the CMO-600 sample, the CMO-700 sample exhibits stronger and more defined Co-O and Mn-O peaks, suggesting that the calcination temperature of 700°C was ideal for forming $CoMn_2O_4$ with high purity, which agrees with previous results. According to the CMO/g-3 curve, the most important characteristic peaks for $CoMn_2O_4$ also were observed in CMO/g-3 sample, indicating that the spinal $CoMn_2O_4$ was well preserved after compositing with graphite.

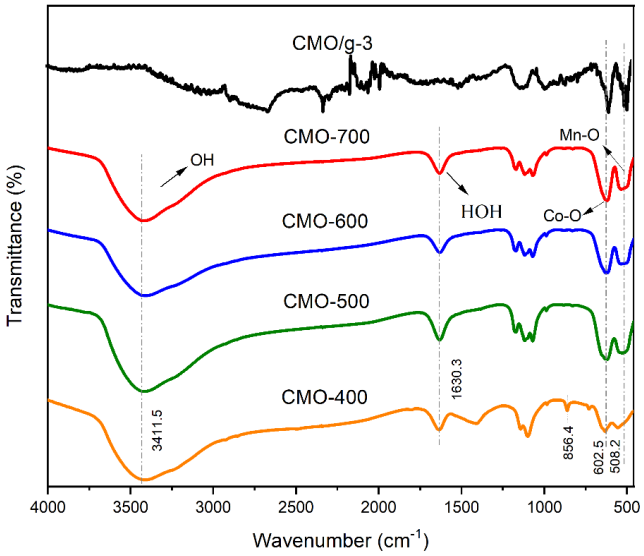

Figure 4. FTIR spectra of CMO-400, CMO-500, CMO-600, CMO-700, and CMO/g-3

3.2 Morphology and specific surface area

The morphology and elemental analysis of CMO-700 and CMO/g-3 were further analyzed using FESEM and EDX analyses, as shown in Figure 5. According to Figure 5a,

* Corresponding to: M. A. A. Mohd Abdah (email: muhammadamirulaizat@utm.my)
DOI: https://doi.org/10.11113/jamst.v30n2.352

the surface of CMO-700 is composed of a great number of stacked nanoparticles with irregular shape, which consist of aggregated tiny nanospheres. Notably, the porous structure of CMO-700 could provide a large electrode/electrolyte contact surface area, whether inside the pores of each microsphere or through channels between the irregular aggregates, which results in more electroactive sites. Secondly, the cycling performance is enhanced due to the more effective strain accommodation during Li^+ insertion and extraction. Moreover, the diffusion path of Li^+ can be shortened[8, 16]. Hence, these structural advantages can enhance the electrochemical performance of the electrode material.

As shown in Figure 5b, the pure graphite sample exhibits a layer structure with a smooth surface. In contrast, in the CMO/g-3, $CoMn_2O_4$ nanoparticles are evenly distributed on the surface or between the layers of graphite, as shown in Figure 5 (c-d). The presence of layered graphite not only enhances the conductivity but also could relieve the severe volume changes during cycling, thereby improving the stability of electrode materials. In addition, the EDX analysis confirms the presence of Co, Mn, O, and C elements in the CMO/g-3, as shown in Figure 5 (g-j). The specific surface area (SSA) of the $CoMn_2O_4$, graphite, and CMO/g-3 was examined based on BET method. BET results indicate that adding graphite to $CoMn_2O_4$ successfully enhanced the SSA to 24.2 m^2 g^{-1}, which can increase the involved electrochemically active sites between the electrode material and the electrolyte during electrochemical reaction if compared to the bare $CoMn_2O_4$ and graphite with 11.8 m^2 g^{-1} and 20.4 m^2 g^{-1}, respectively[17, 18].

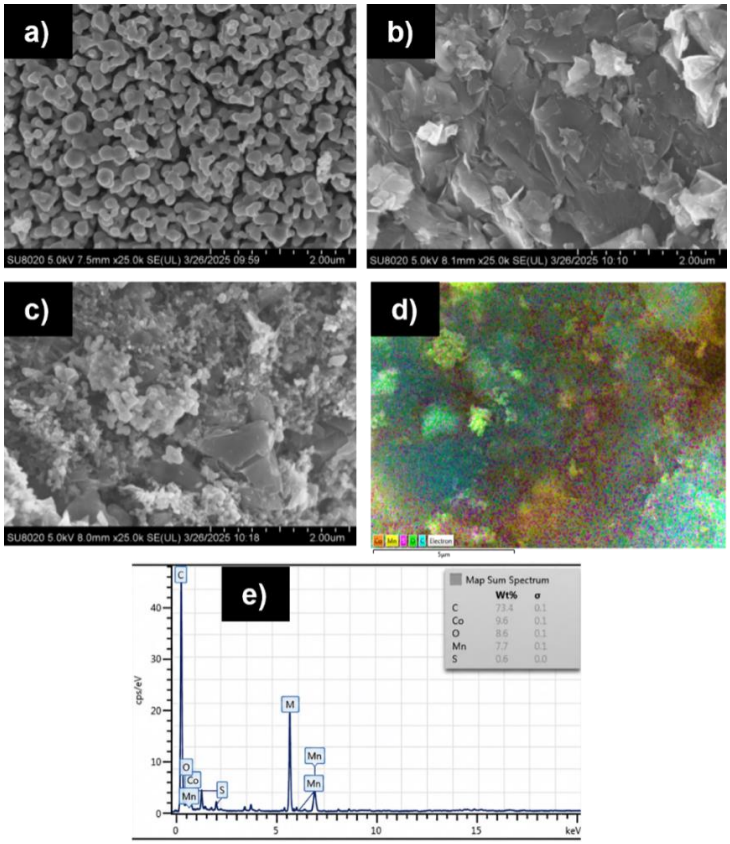

Figure 5. FESEM images of (a) CMO-700, (b) graphite, (c) CMO/g-3 electrode. (d) EDX mappings and (e) elemental distribution of CMO/g-3 electrode

* Corresponding to: M. A. A. Mohd Abdah (email: muhammadamirulaizat@utm.my)
DOI: https://doi.org/10.11113/jamst.v30n2.352

3.3 Electrochemical measurements

The Li^+ storage mechanism of CMO/g-3 electrode was studied via cyclic voltammetry (CV) curves at a scan rate of 0.1 mV s^{-1} in the voltage range from 0-3 V for three cycles, as shown in Figure 6a. During the first cathodic sweep, a reduction peak appears at approximately 0.25 V, which disappears in subsequent cycles. This peak is associated with the initial of lithium ions (Li^+) within the mesoporous structure of graphite, meanwhile the prominent oxidation peak at ~0.3 V corresponds to the Li^+ from the graphite layer [19]. The peak observed at approximately 1.3 V corresponds to the reduction of Mn^{3+} to Mn^{2+}, along with the formation of the solid electrolyte interphase (SEI) layer [20]. The cathodic peak at 1.0 V is attributed to two reduction reaction: the in-situ formed Mn^{2+} is further reduced to Mn^0 and Co^{2+} is directly reduced to Co^0.

In the anodic scan, two oxidation peaks at 1.6 V and 2.0 V corresponded to the oxidation of Mn and Co to MnO and CoO, respectively. In the subsequent cycles, these two peaks displayed a slight potential shift [17]. Based on the above analysis, the Li^+ storage mechanism in the CMO/g-3 electrode composite could be described as follows:

$$CoMn_2O_4 + 8Li^+ + 8e^- \rightarrow Co + 2Mn + 4Li_2O \quad (8)$$

$$Co + 2Mn + 3Li_2O \leftrightarrow CoO + 2MnO + 6Li^+ + 6e^- \quad (9)$$

After the first cycle, the CV curves of the CMO/g-3 electrode stabilize and show no significant changes in the following scans, indicating good electrochemical reversibility [21].

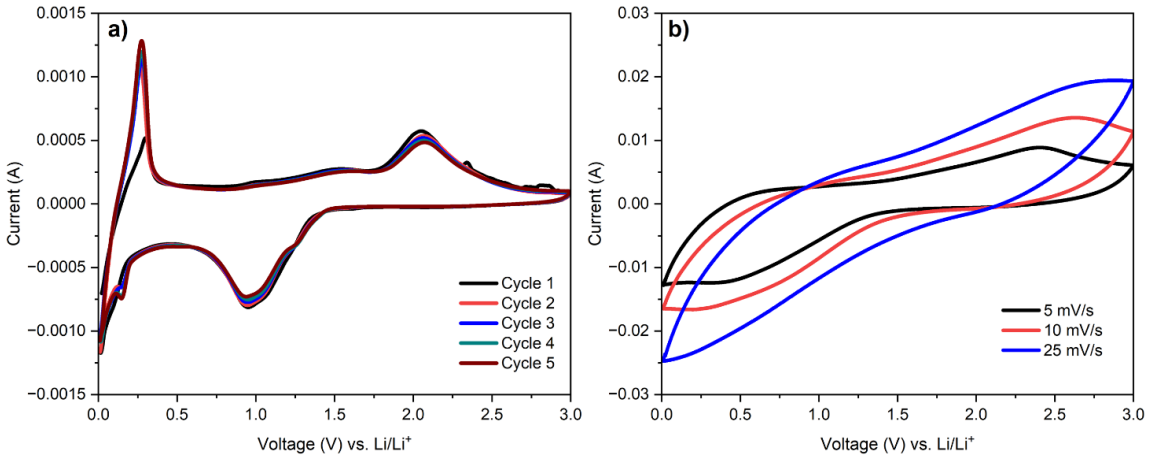

Figure 6. (a) Cyclic voltammetry curves for CMO/g-3 half-cell electrode at potential range 0-3V *vs.* Li/Li^+, at the scan rate of 0.1 mV s^{-1}. (b) CV curves of CMO/g-3 half-cell at various scan rates

Figure 7a-d illustrates the electrochemical behavior of the CMO/g-3 electrode, focusing on the relationship between scan rates (based on Figure 6b), current response, and the contributions of diffusion-controlled and diffusion-limited processes. Figure 7a shows a logarithmic plot of the peak current versus scan rate. The linear relationship was observed

* Corresponding to: M. A. A. Mohd Abdah (email: muhammadamirulaizat@utm.my)
DOI: https://doi.org/10.11113/jamst.v30n2.352

with a slope of 0.45294 and an R^2 value of 0.93659. A slope close to 0.5 typically represents a purely diffusion-controlled process, while a slope near 1 indicates capacitive behavior [22]. The finding portrays a b-value of 0.45, signifying that the electrochemical process is predominantly a diffusion-controlled process [23]. Figure 7b presents a plot of $i_p / \nu^{1/2}$ versus $\nu^{1/2}$, which follows the Randles–Sevcik relationship. The high linearity (R^2 = 0.99982) confirms that the system is under a well-defined diffusion-controlled regime at varying scan rates [24]. The negative slope (-2.82361) indicates the decreasing contribution of diffusion processes at higher scan rates, consistent with typical electrochemical behavior where faster scan rates reduce diffusion control [25, 26]. Notably, the relative contributions of diffusion and diffusion-limited processes at different scan rates were quantified at Figure 7c.

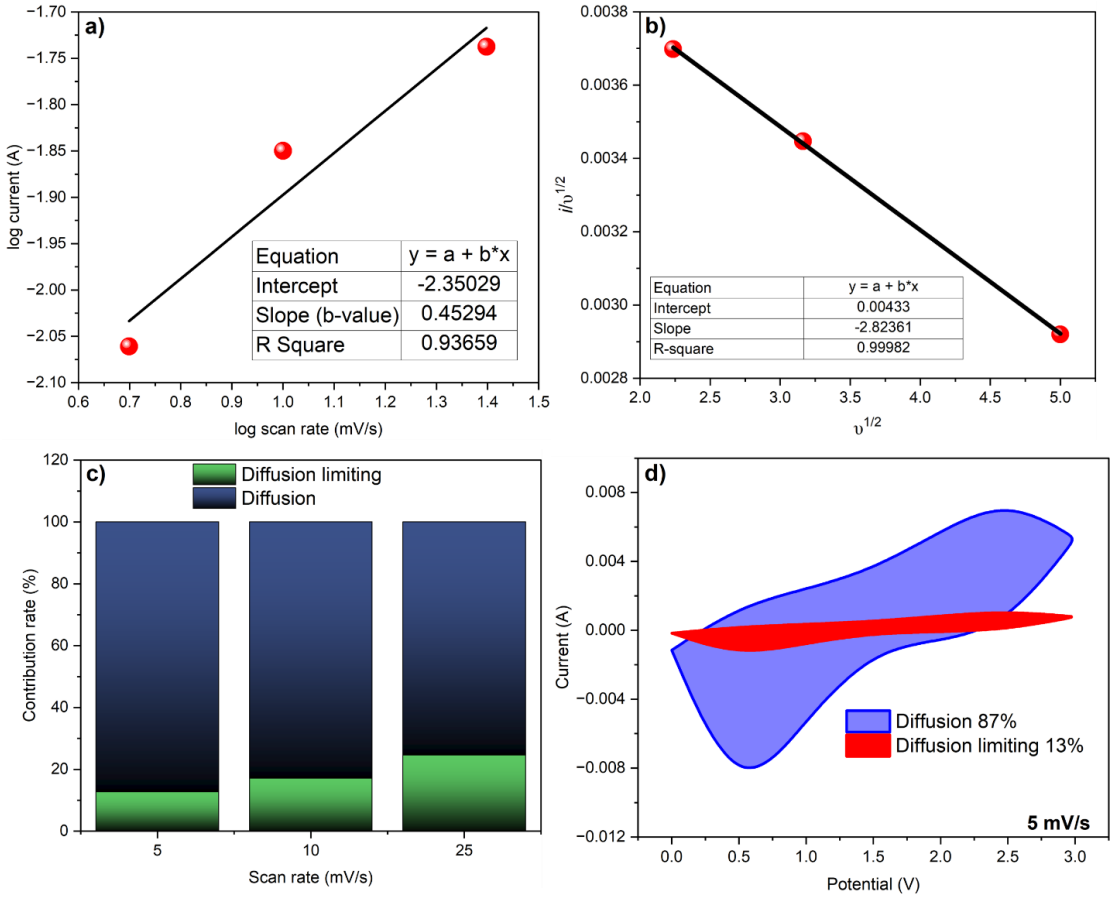

Figure 7. (a) log scan rate (mV/s) versus log current (A), (b) $\nu^{1/2}$ versus $i/\nu^{1/2}$, (c) Histogram of diffusion and diffusion limiting contribution ratio at different scan rates and (d) Percentage of diffusion and diffusion limiting contribution of CMO/g-3 electrode at 5 mV/s

At low scan rates (5 mV/s), diffusion-controlled processes dominate (~87%), whereas the diffusion-limited contribution is minimal (~13%). As the scan rate increases to 25 mV/s, the diffusion-limited contribution increases slightly, suggesting that higher scan rates enhance the capacitive response relative to the diffusion-controlled behavior [25, 26].

* Corresponding to: M. A. A. Mohd Abdah (email: muhammadamirulaizat@utm.my)
DOI: https://doi.org/10.11113/jamst.v30n2.352

This trend confirms that the $CoMn_2O_4$/graphite electrode exhibits both surface-controlled and diffusion-dominated electrochemical kinetics, which can be attributed to the intrinsic battery-type redox behavior of $CoMn_2O_4$ [27] and the highly conductive, carbonaceous nature of graphite [28].

Figure 7d provides a visual representation of the contribution percentages at a fixed scan rate of 5 mV/s. The majority of the current originates from diffusion-controlled processes (blue region, 87%), while a minor portion arises from diffusion-limited contributions (red region, 13%). This distribution highlights the efficient electrochemical accessibility of the active sites in the composite and suggests favorable charge transport within the material. Overall, the electrochemical analysis confirms that the composite exhibits mixed charge storage behavior, with diffusion-controlled processes being dominant at low scan rates. This behavior is crucial to support the implementation of CMO/g-3 electrode in lithium-ion battery applications that required both high-rate capability and stable charge storage.

Figure 8a provides the cycling performance of CMO/g-0, CMO/g-1, CMO/g-2, CMO/g-3 at 0.1A g^{-1} for 100 cycles. CMO/g-0 and CMO/g-1 electrode showed similar initial specific capacity around 500 mAh g^{-1}, while CMO/g-2 and CMO/g-3 exhibits superior initial discharge specific capacity of 2246 mAh g^{-1} and 2503 mAh g^{-1}, respectively. The increase in capacity is contribution to the amount of $CoMn_2O_4$, which improve the overall specific capacity of electrode materials. In initial 10 cycles, the capacity of CMO/g-3 drop obviously, while in the subsequent cycles the decline slow down and finally keeps stabilized, which means need few cycles to form stable SEI film. And the irreversible capacity loss due to the information of SEI film and irreversible reaction of $CoMn_2O_4$ into MnO and CoO [11].

After 100 cycles, CMO/g-3 electrode still release the highest reversible specific capacity around 1000 mAh g^{-1} compared to CMO/g-0 (352.19 mAh g^{-1}), CMO/g-1 (316.68 mAh g^{-1}), CMO/g-2 (695.48 mAh g^{-1}), respectively. The discharge performance of CMO/g electrodes before and after cycling is summarized in Table 1. According to Figure 8b, the coulombic efficiency for CMO/g-3 is constantly remain around 100% from 2 to 100 cycles. Rate performance of CMO/g-3 were tested at different current density from 0.1 A g^{-1} to 0.5 A g^{-1} (Figure 8c). The average discharge specific capacities of the electrode materials were calculated to be 2036.8 $mAhg^{-1}$, 1037.6 mAh g^{-1}, 683.4 mAh g^{-1}, 503.1 mAh g^{-1}, 364.9 mAh g^{-1} for 0.1A g^{-1}, 0.2A g^{-1}, 0.3A g^{-1}, 0.4A g^{-1}, and 0.5A g^{-1}, respectively. Table 2 summarizes the discharge performance of the CMO/g-3 electrode at different current densities. When current density returns to 0.1 A g^{-1}, the discharge specific capacity of electrode does not show obvious degradation, indicating that the CMO/g-3 electrode possesses excellent rate performance.

* Corresponding to: M. A. A. Mohd Abdah (email: muhammadamirulaizat@utm.my)
DOI: https://doi.org/10.11113/jamst.v30n2.352

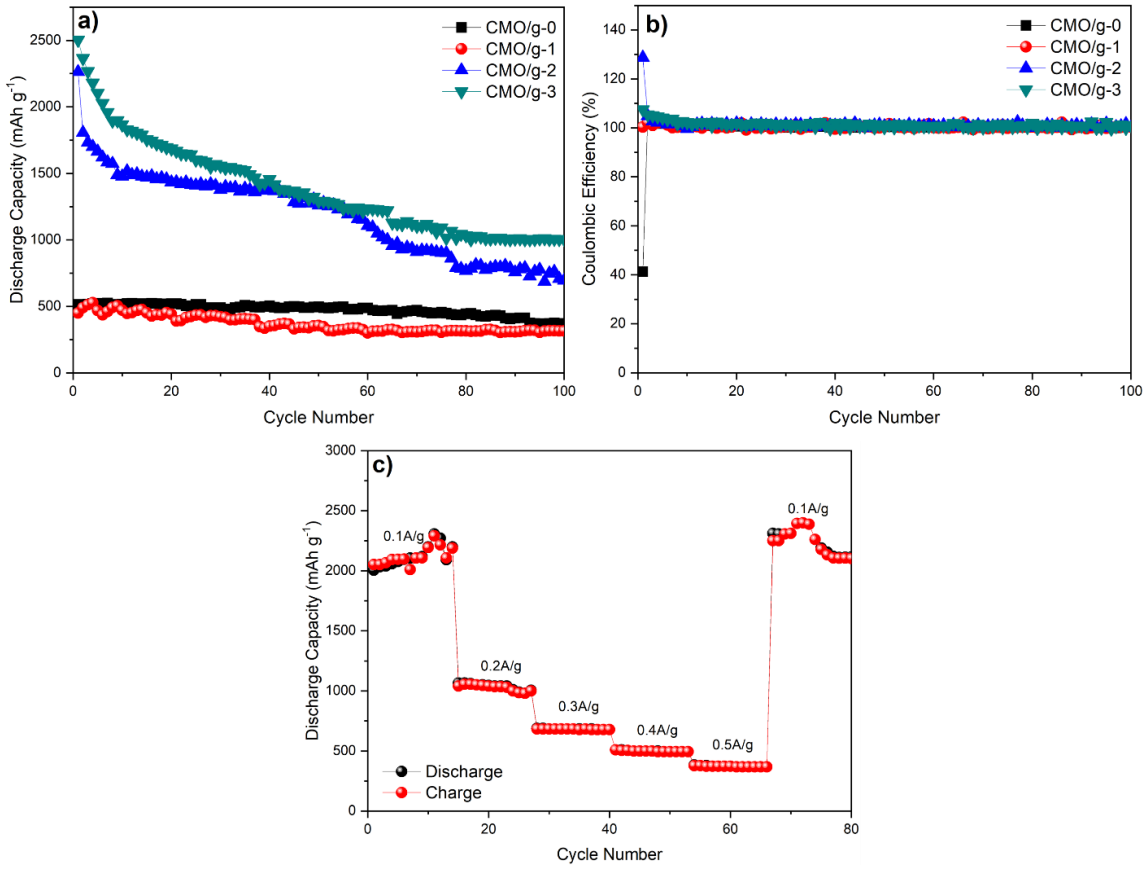

Figure 8. (a) Cycling performance and (b) coulombic efficiencies of CMO/g-0, CMO/g-1, CMO/g-2, CMO/g-3 at a current density of 0.2 A g^{-1} for 100 cycles. (c) Rate performance of CMO/g-3 electrode at various current densities

Table 1. Discharge specific capacity of $CoMn_2O_4$/graphite electrodes before and after cycling

Electrodes	First discharge specific capacity ($mAhg^{-1}$)	Discharge specific capacity (100^{th} cycle, $mAhg^{-1}$)
CMO/g-0	508.2	358.1
CMO/g-1	461.8	349.9
CMO/g-2	2263.4	689.8
CMO/g-3	2503.6	1022.0

* Corresponding to: M. A. A. Mohd Abdah (email: muhammadamirulaizat@utm.my)
DOI: https://doi.org/10.11113/jamst.v30n2.352

Table 2. Discharge and charge specific capacities of CMO/g-3 electrode at different currents densities

Current density (A g^{-1})	Discharge specific capacity (mAh g^{-1})	Charge specific capacity (mAh g^{-1})
0.1	2036.8	2053.7
0.2	1037.6	1028.1
0.3	683.4	689.8
0.4	503.1	503.1
0.5	364.9	364.9
0.1	2114.3	2114.2

To investigate the reaction kinetic behavior of the all CMO/g electrodes, EIS tests were performed on the all samples before and after 100 cycles, over a frequency range from 1 kHz to 1 Hz. All EIS curves show a semicircle in the high-frequency region, which corresponds to the charge transfer resistance (R_{ct}) and the inclined line in the low frequency which corresponds to the Warburg diffusion process (Z_w). R_s was corresponded to the resistance of electrolytes, exhibited in the intercept of high frequency of Z' axis[13, 29]. According to the Nyquist plots in Figure 9a, the initial R_{ct} values are CMO/g-0 (15.71 Ω), CMO/g-1 (54.31 Ω), CMO/g-2 (56.41 Ω), CMO/g-3 (12.28 Ω), respectively. After 100 cycles (Figure 9b), CMO/g-3 still exhibits the lowest R_{ct} of 86.19 Ω compared to CMO/g-1 (260.67 Ω), CMO/g-2 (338.53 Ω). This result indicates that CMO/g-3 displays the least charge transfer resistant and highest electrical conductivity, which is due to the uniform distribution of $CoMn_2O_4$ on the graphite surface and the high surface area of graphite that increases the electrochemical reaction active sites. Table 3 presents the electrochemical impedance results of $CoMn_2O_4$/graphite electrodes obtained from the Nyquist plots before and after cycling.

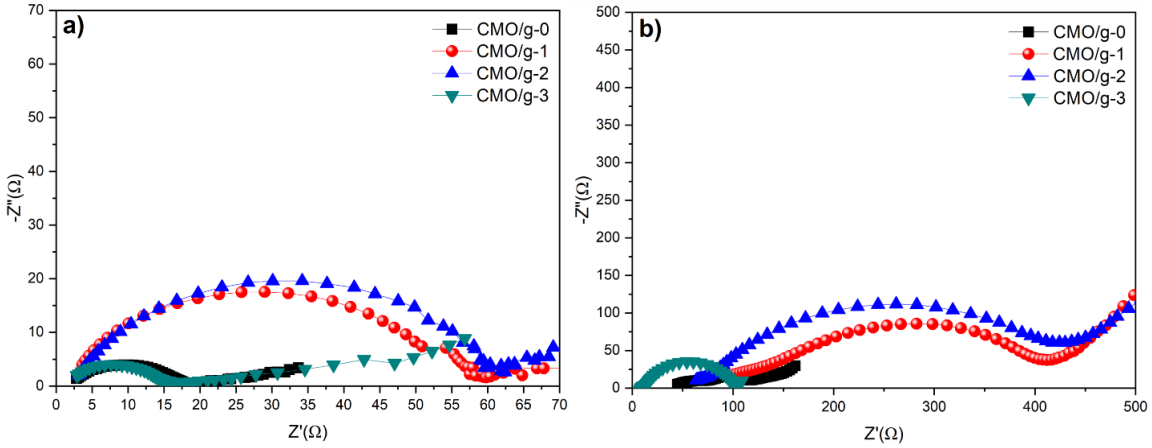

Figure 9. Nyquist plots of CMO/g-0, CMO/g-1, CMO/g-2, CMO/g-3 (a) before and (b) after cycling, respectively

* Corresponding to: M. A. A. Mohd Abdah (email: muhammadamirulaizat@utm.my)
DOI: https://doi.org/10.11113/jamst.v30n2.352

Table 3. Electrochemical impedance parameters of $CoMn_2O_4$/graphite electrodes measured from the Nyquist plot before and after cycling.

Electrodes	R_{ct} (before cycling, Ω)	R_{ct} (after cycling, Ω)	R_s (before cycling , Ω)	R_s (after cycling , Ω)
CMO/g-0	15.71	73.8	1.39	56.98
CMO/g-1	54.31	260.67	3.61	133.68
CMO/g-2	56.41	338.53	3.12	80.04
CMO/g-3	12.28	86.19	2.88	9.58

To assess the practical feasibility of the as-prepared CMO/g-3 anode, a full lithium-ion battery was assembled using CMO/g-3 as the anode and commercial $LiFePO_4$ (LFP) as the cathode, as illustrated in Figure 10. The corresponding discharge capacities and coulombic efficiencies (CE) of the CMO/g-3//LFP full cell are presented in Figure 10a. The device delivers an initial discharge capacity of 146.5 mAh g^{-1} at a current density of 0.2 A g^{-1}. Considering the theoretical specific capacity of $LiFePO_4$ (170 mAh g^{-1}, corresponding to its theoretical 1C capacity), the obtained capacity represents approximately 86.2% of the theoretical capacity of $LiFePO_4$. However, after 100 charge–discharge cycles, the capacity decreases to 64.5 mAh g^{-1}, corresponding to a retention of only ~44%. This pronounced capacity fading can be mainly attributed to the substantial volume variation of the electrode during repeated lithiation and delithiation processes. Such volumetric expansion induces severe pulverization of the active material, accompanied by continuous degradation of the solid electrolyte interphase (SEI) layer and ongoing electrolyte consumption. The assembled CMO/g-3//LFP full cell exhibits a relatively small initial irreversible capacity loss (ICL) of approximately 11%, which is likely associated with SEI formation on the electrode surface as well as the irreversible reduction of surface functional groups [30]. Despite this initial loss, the CE rapidly approaches nearly 100% upon further cycling, indicating highly reversible electrochemical reactions after stabilization [31].

To further elucidate the reaction kinetics, electrochemical impedance spectroscopy (EIS) measurements were performed on the full cell before and after cycling (Figure 10b). Prior to cycling, the cell displays a solution resistance (R_s) of ~7.9 Ω and a charge-transfer resistance (R_{ct}) of ~154 Ω. After cycling, a noticeable increase in R_{ct} to 463 Ω was observed, which can be attributed to pronounced volume fluctuations arising from the lithium alloying/dealloying process. The repeated expansion and contraction generate mechanical stress within the electrode, leading to structural disintegration and accelerated capacity decay [32], which is consistent with the poor cycling stability observed in Figure 10a. Moreover, excessive volume swelling can cause mechanical fracture and loss of electrical contact between the active material and the current collector, further compromising the long-term electrochemical performance of the battery [33]. Conversely, the R_s decreased from ~7.9 Ω to ~3.3 Ω after cycling, implying an increase in electrolyte conductivity upon repeated charge–discharge cycles [34].

* Corresponding to: M. A. A. Mohd Abdah (email: muhammadamirulaizat@utm.my)
DOI: https://doi.org/10.11113/jamst.v30n2.352

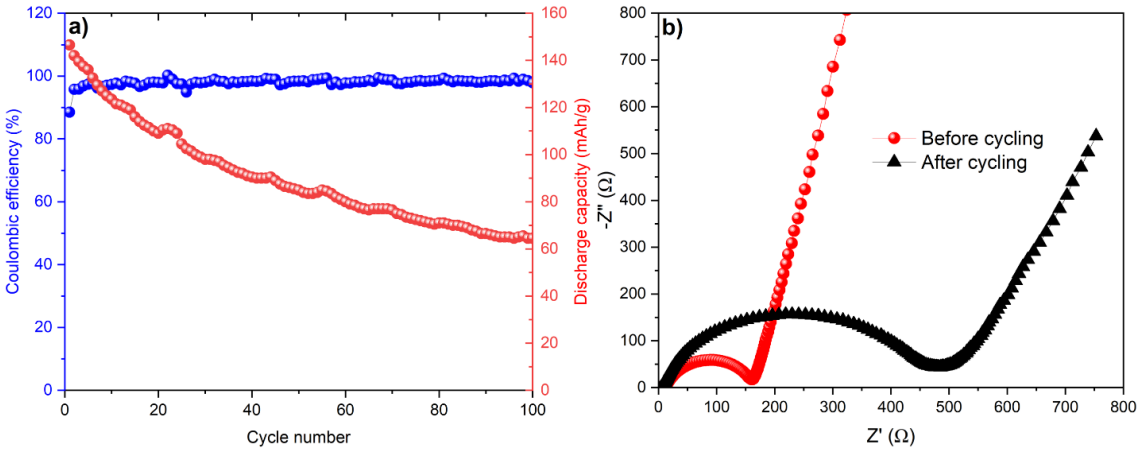

Figure 10. (a) Cycling performances of CMO/g-3/LFP at 0.2 A g^{-1}. (b) Nyquist plots measured for CMO/g-3/LFP before and after cycling

4.0 CONCLUSION

In this study, $CoMn_2O_4$ was successfully synthesized via a hydrothermal method followed by calcination, as confirmed by XRD, FTIR, and FESEM-EDX analyses. Among the prepared samples, CMO-700 exhibited the highest crystallinity and a porous structure, making it suitable for electrochemical applications. When composited with graphite, the CMO/g-3 sample showed uniform distribution of $CoMn_2O_4$ on the graphite surface and demonstrated the best electrochemical performance. The synergistic effect between $CoMn_2O_4$ and graphite effectively enhanced the specific capacity while improving cycling stability. CMO/g-3 delivered a high initial discharge capacity of 2503 mAh g^{-1} and maintained around 1000 mAh g^{-1} upon prolonged cycling. It also exhibited the lowest charge-transfer resistance before and after cycling, indicating improved reaction kinetics and structural stability. In the assembled CMO/g-3//LFP full cell, an initial discharge capacity of 146.5 mAh g^{-1} was achieved at 0.2 A g^{-1}. However, capacity retention decreased after 100 cycles due to significant volume expansion of the anode, leading to increased resistance and structural degradation. Despite this limitation, the full cell showed low initial irreversible capacity loss and coulombic efficiency close to 100% in subsequent cycles, reflecting good reversibility. Overall, the $CoMn_2O_4$/graphite composite, particularly CMO/g-3, demonstrates promising potential as a high-capacity anode material, although further improvement in cycling stability is required for practical lithium-ion battery applications.

DECLARATION OF COMPETING INTEREST

The authors declare no conflict of interest.

ACKNOWLEDGEMENT

The authors gratefully acknowledge Geran Penyelidikan Hi-Tech(F4) (Q.J130000.4654.00Q25) for supporting this research. The authors also acknowledge the

* Corresponding to: M. A. A. Mohd Abdah (email: muhammadamirulaizat@utm.my)
DOI: https://doi.org/10.11113/jamst.v30n2.352

Advanced Membrane Technology Research Centre (AMTEC), UTM, for providing the electrochemical analysis for battery testing.

REFERENCES

[1] Lin, S., & Zhang, T. (2024). Preparation of various Co/Cu and Co/Fe molar ratios and gel-modified nanomaterials as anodes for Li-ion batteries. *Materials Chemistry and Physics, 311*, 128547.

[2] International Energy Agency. (2022). *World energy outlook 2022*. International Energy Agency.

[3] Raimi, D., & Newell, R. G. (2024). *Global energy outlook comparison methods: 2023 update*.

[4] Cai, W., Yao, Y.-X., Zhu, G.-L., Yan, C., Jiang, L.-L., He, C., Huang, J.-Q., & Zhang, Q. (2020). A review on energy chemistry of fast-charging anodes. *Chemical Society Reviews, 49*(12), 3806–3833.

[5] Elalfy, D. A., Gouda, E., Kotb, M. F., Bureš, V., & Sedhom, B. E. (2024). Comprehensive review of energy storage systems technologies, objectives, challenges, and future trends. *Energy Storage Research, 54*, 101482.

[6] Li, M.-T., Liu, R.-R., Wang, L.-Y., Wang, H.-J., Sun, J.-W., & Yu, Y. (2025). Iron-based bimetallic oxide carbon composites with superior lithium storage capabilities serve as anode in lithium-ion batteries. *Inorganic Chemistry Communications, 574*, 122399.

[7] Cai, K.-X., Luo, S.-H., Jun, C., Kun, L., Yan, S.-X., Hou, P.-Q., Qing, W., Zhang, Y.-H., & Xin, L. (2023). Enhancement of lithium storage performance of $ZnMn_2O_4$ anode by optimizing hydrothermal synthesis. *Transactions of Nonferrous Metals Society of China, 33*(9), 2772–2783.

[8] Sanad, M., Yousef, A. K., Rashad, M., Naggar, A., & El-Sayed, A. (2020). Robust and facile strategy for tailoring $CoMn_2O_4$ and $MnCo_2O_4$ structures as high-capacity anodes for lithium-ion batteries. *Polyhedron, 579*, 411889.

[9] Shi, Y. J., Song, M. J., Zhang, Y., Zhang, C., Gao, H., Niu, J. Z., Ma, W. S., Qin, J. Y., & Zhang, Z. H. (2019). A self-healing $CuGa_2$ anode for high-performance Li-ion batteries. *Journal of Power Sources, 437*, 226916.

[10] Shen, M., & Ma, H. (2022). Metal-organic frameworks (MOFs) and their derivatives as electrode materials for lithium-ion batteries. *Coordination Chemistry Reviews, 470*, 214715.

[11] Zhang, D., Zhang, C. Y., Xu, H. S., Huo, Z., Shi, X. Y., Luo, B. M., Liu, G. Y., Liu, X. D., Li, L. P., & Yu, C. (2024). Ultrafast synthesis of spinel AMn_2O_4 (A = Co, Mn, Zn) nanopolyhedras and their composites applied to lithium-ion battery anode. *Journal of Alloys and Compounds, 987*, 174040.

[12] Pan, X., Ma, J., Yuan, R., & Yang, X. (2017). Layered double hydroxides for preparing $CoMn_2O_4$ nanoparticles as anodes of lithium-ion batteries. *Materials Chemistry and Physics, 194*, 137–141.

[13] Abdah, M. A. A. M., Azlan, F. N. M., Wong, W. P., Mustafa, M. N., Walvekar, R., & Khalid, M. (2024). Microwave-assisted upcycling of plastic waste to high-performance carbon anode for lithium-ion batteries. *Chemosphere, 349*, 140973.

* Corresponding to: M. A. A. Mohd Abdah (email: muhammadamirulaizat@utm.my)
DOI: https://doi.org/10.11113/jamst.v30n2.352

[14] Yao, B., Wang, Z., Ding, C., Feng, M., Li, Z., & Huang, Y. (2023). $ZnFe_2O_4$/Graphite composite with high performance as anode material for lithium-ion batteries. *Energy Materials Letters, 19*(1), 29–37.
[15] Murugesan, M., Nallamuthu, N., Ranjithkumar, R., Krishnakumar, M., Devendran, P., & Ramesh, K. (2023). Synthesis and electrochemical investigation of hetero-bimetallic $CoMn_2O_4$ microrods for novel supercapacitor electrodes. *Energy Materials Letters, 19*(1), 108–118.
[16] Azad, A. K., Abdalla, A. M., Kumarasinghe, P. I. I., Nourean, S., Azad, A. T., Ma, J., Jiang, C., Dawood, M. M. K., Wei, B., & Patabendige, C. N. K. (2024). Developments and key challenges in micro/nanostructured binary transition metal oxides for lithium-ion battery anodes. *Journal of Energy Storage, 84*, 110850.
[17] Wang, W., Zhang, P., Jiang, X., Zhou, J.-J., Xu, L., Chen, F., & Chen, L. (2022). Constructing N-doped carbon beads-encapsulated $CoMn_2O_4$ microboxes with pyramidal walls for enhanced Li storage. *Materials Today Energy, 30*, 101149.
[18] Nakhodchari, M. M., Seifi, M., & Moghadam, M. T. (2023). Ternary $MnCo_2O_4$/MWCNT/rGO nanocomposites as high-performance supercapacitor electrode materials. *Journal of Physics and Chemistry of Solids, 174*, 111170.
[19] Rong, T., Yuan, Y., Yu, H., Zuo, H., & Xue, Q. (2023). Research on anthracite-derived graphite flakes prepared by molten salt electrolysis as anode materials for high-performance lithium-ion batteries. *Fuel Processing Technology, 252*, 107992.
[20] Feng, J., Zhang, B., Du, P., Yuan, Y., Li, M., Chen, X., Guo, Y., Xie, H., & Yin, H. (2023). Recovery of $LiCoO_2$ and graphite from spent lithium-ion batteries by molten-salt electrolysis. *iScience, 26*(11), 108097.
[21] Abdah, M. A. A. M., Mokhtar, M., Khoon, L. T., Sopian, K., Dzulkurnain, N. A., Ahmad, A., Sulaiman, Y., Bella, F., & Su'ait, M. S. (2021). Synthesis and electrochemical characterizations of poly(3,4-ethylenedioxythiophene)/manganese oxide coated on porous carbon nanofibers as a potential anode for lithium-ion batteries. *Energy Reports, 7*, 8677–8687.
[22] Saidi, N. M., Khairudin, A., Mustafa, M. N., Omar, F. S., Gerard, O., Tan, Y. S., Khalid, M., & Numan, A. (2024). Highly amorphous cobalt phosphate synthesized via microwave route as a superior positive electrode material for asymmetric supercapatteries. *Journal of Energy Storage, 97*, 112647.
[23] Mustafa, M. N., Abdah, M. A. A. M., Numan, A., Sulaiman, Y., Walvekar, R., & Khalid, M. (2023). Effect of precursor concentration on the electrochemical properties of nickel cobalt phosphate for high-performance electrochromic supercapacitors. *Journal of Energy Storage, 74*, 109321.
[24] Mundinamani, S., & Rabinal, M. K. (2014). Cyclic voltammetric studies on the role of electrode, electrode surface modification and electrolyte solution of an electrochemical cell. *IOSR Journal of Applied Chemistry, 7*, 45–52.
[25] Saidi, N. M., Khairudin, A., Li, L., Abdah, M. A. A. M., Gerard, O., Tan, Y. S., Khalid, M., Khan, F., Mustafa, M. N., & Numan, A. (2023). Performance comparison of 2D nickel phosphate nanoparticles prepared via sonochemical and microwave-assisted hydrothermal routes for supercapattery. *Journal of Energy Storage, 73*, 108846.
[26] Gerard, O., Ramesh, S., Ramesh, K., Numan, A., Mustafa, M. N., Khalid, M., Ramesh, S., & Tiong, S. K. (2024). Evaluation of the effect of precursor ratios on the

* Corresponding to: M. A. A. Mohd Abdah (email: muhammadamirulaizat@utm.my)
DOI: https://doi.org/10.11113/jamst.v30n2.352

electrochemical performances of binder-free NiMn-phosphate electrodes for supercapattery. *Journal of Colloid and Interface Science, 667*, 585–596.

[27] Mijailović, D. M., Radmilović, V. V., Lačnjevac, U. Č., Stojanović, D. B., Bustillo, K. C., Jović, V. D., Radmilović, V. R., & Uskoković, P. S. (2021). Tetragonal $CoMn_2O_4$ nanocrystals on electrospun carbon fibers as high-performance battery-type supercapacitor electrode materials. *Dalton Transactions, 50*(43), 15669–15678.

[28] Deng, J., Liu, C., Chen, X., & Madou, M. (2026). Mechanically strong and highly conductive graphitized carbon nanowire arrays for nano-fabrication of carbon-based chips. *Microsystems & Nanoengineering, 12*(1), 30.

[29] Kanagambal, P., Ahamed, A. J., & Rajeswaran, P. (2023). A novel mesoporous $CoMn_2O_4$@rGO composite as an electrode material for hybrid supercapacitor energy storage device applications. *Diamond and Related Materials, 137*, 110098.

[30] Mohd Abdah, M. A. A., Mohammad Azlan, F. N., Wong, W. P., Mustafa, M. N., Walvekar, R., & Khalid, M. (2024). Microwave-assisted upcycling of plastic waste to high-performance carbon anode for lithium-ion batteries. *Chemosphere, 349*, 140973.

[31] Mohd Abdah, M. A. A., Mohammad Azlan, F. N., Wong, W. P., Mustafa, M. N., Numan, A., Walvekar, R., & Khalid, M. (2025). Enhancing sustainable lithium-ion battery anode using activated carbon-derived polypropylene plastic waste/MXene hybrid composite. *Journal of Electroanalytical Chemistry, 997*, 119472.

[32] Sunjaya, N. B. P., Yulianti, R. T., Hanifah, A., Fadila, S., Indriyati, I., Priyono, S., Indayaningsih, N., Setiawan, J., Effendi, M., & Yudianti, R. (2026). Structural and synergistic effect of SnO_2–carbon interfaces for improved lithium-ion battery anode performance. *Surfaces and Interfaces, 83*, 108502.

[33] Min, K., Kim, K., An, H., Go, Y., Lee, Y., Lim, D., & Baeck, S.-H. (2022). Yolk-shell-structured SiO_2@N,P co-doped carbon spheres as highly stable anode materials for lithium-ion batteries. *Journal of Power Sources, 543*, 231849.

[34] Cifre-Herrando, M., Roselló-Márquez, G., & García-Antón, J. (2025). Structural and electrochemical characterization of modified WO_3 nanostructures for lithium-ion battery anodes. *Separation and Purification Technology, 373*, 133673.

* Corresponding to: M. A. A. Mohd Abdah (email: muhammadamirulaizat@utm.my)
DOI: https://doi.org/10.11113/jamst.v30n2.352